OVERHEATING INDUCED BY AL-SI COATING DURING SPOT WELDING OF A DISSYMMETRICAL THREE SHEETS ASSEMBLY

E. GESLAIN*, P. ROGEON*, T. PIERRE*, C. POUVREAU* and L. CRETTEUR**

** Université Bretagne Sud,IRDL,UMR CNRS 6027, Lorient, France*
*** ArcelorMittal Global R&D, Montataire, France*

DOI 10.3217/978-3-85125-615-4-38

ABSTRACT

In automotive industry, the lightweight of body in white is a challenge to meet environmental standards. Where some car manufacturers favour lighter materials, steel is always more economical and easy to assemble by resistance welding. Thus, the tendency is to reduce the thickness of cover sheets and use advanced high strength steel in better position for the structure. The press-hardened steels (of hot-pressed forming steel) are also a key of lightweight. The manufacturing of the body in white requires various combinations of different steel sheets that can induce weldability issues when using resistance spot welding process.

This work aims at understanding the mechanisms that influence the initiation and the growing of the nugget in a specific combination with three dissimilar coated steel sheets. The stack-up includes a very thin (0.57 mm) zinc coated low carbon steel sheet, a thick (1.47 mm) zinc coated advanced high strength steel sheet, and a thick (1.2 mm) aluminum-silicon coated press hardened steel sheet. The aluminum-silicon coating is transformed during hot stamping process and becomes more resistive.

A numerical 2D axisymmetric electro-thermal model developed with COMSOL Multiphysics® is used here to improve the knowledge of the thermal phenomena occurring during the first times of the welding stage. Specific attention is paid to the contact conditions at both macroscopic and microscopic scales. Contact radii evolutions issued from experimental observations are considered in the model. Thermal and electrical contact resistances evolutions experimentally measured versus stress and temperature are also considered in the model.

The model is consistent with several experimental observations issued from infrared images and voltage between the electrodes. It confirms the intense heating observed by infrared camera at the level of the two interfaces with the PHS sheet, because of the high contact resistances induced by the aluminum-silicon coating. Consequently, the nugget appears quickly inside the PHS sheet.

Keywords: resistance spot welding, contact resistances, infrared thermography

INTRODUCTION

Advanced high strength steels are developed to gain weight and safety on new vehicles for automotive application. Steel sheets tend to become thinner to follow the environmental goals by reducing the weight of material. The resistance spot welding (RSW) process is largely optimized to join assemblies with similar steel sheets but difficulties could happen with dissymmetrical assemblies: the ones combining different sheets with different thicknesses, different steel grades, and different coatings. This work deals with the understanding of the mechanisms that influence the overheating observed at the beginning of welding of a very dissymmetrical assembly of three steel sheets. The stack-up includes a very thin zinc coated low carbon steel (LCS) sheet, a zinc coated advanced high strength steel (AHSS) sheet, and a press hardened steel (PHS) with Al-Si coating. By applying standard RSW conditions, there is a high probability that the thin LCS sheet will not be welded. An attempt to understand the effect of the contact conditions on the initial heats through numerical and experimental approaches is proposed in this article. An electro-thermal model is used here for the numerical simulation of the phenomena during the first 50 ms of welding.

Recent works already mention weldability problems when joining by RSW three sheet assemblies combining a thin mild steel sheet and high strength steel thicker sheets [1], [2]. The use of different material combinations with different coatings, and different sheet thicknesses in the three layers complicates drastically the weldability of the combinations of steel sheets. The authors report difficulties to find the right operating conditions to encourage the nugget development toward the thin sheet. Nielsen et al. find that the thin sheet is dominantly welded to the thicker by bonding diffusion [1]. Huda et al. were particularly interested by three-sheet stacks with a thick Al-Si coated steel (AL-HPF) sheet [2]. They show from macrographs that significant heating occurs at the interfaces of the Al-Si coated sheet, placed at the centre of the three-sheet stack. This coating appears to have an important role in the heating process.

Several relevant works [3]–[8] have already highlighted through numerical approaches the importance of contact conditions in the case of dissimilar assemblies. The nature of the coating on the sheets influences mainly the contact conditions. With galvanized steel sheets, electrical contact resistance at the faying interface is strongly reduced compared to the case with non-coated sheets [9]. Füssel et al. [10] have used a specific welding device to observe by infrared (IR) camera the development of the nugget inside sheets stack. The method consists in squeezing and welding the border of the steel sheets stack with half electrodes to open the welding area and provide to the camera with an observation angle. They have compared heating development filmed by IR camera and obtained by numerical simulations.

We have designed an experimental apparatus to reproduce a RSW operation and to allow observation of heating process by IR camera. A finite element model has been developed with COMSOL Multiphysics®. It is a coupled electro-thermal model with contact radii evolution. An important work has been done concerning the modelling of the contact conditions.

Half-spot IR images are compared with numerical simulation in the first milliseconds of welding to link higher contact resistance with faster heating. Numerical voltage calculated between electrodes are also confronted to measurements.

EXPERIMENTAL WORK

MATERIAL

The welding tests are achieved with a GYSPOT® medium frequency direct current welding machine developed for automotive body repair. A structure has been designed to maintain the welding gun in a horizontal position and the IR camera above in a vertical position (Fig. 1).

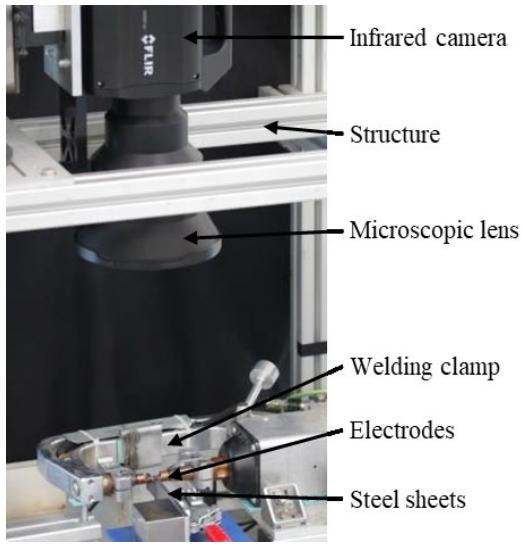

Fig. 1 Specific welding device with the IR camera to observe the welding area.

Welding electrodes are in copper-chromium-zirconium alloy with a 32 mm contact radius and a 13 mm diameter. They are milled on 6 mm depth at the half of diameter (Fig. 2). The support of electrodes is water-cooled.

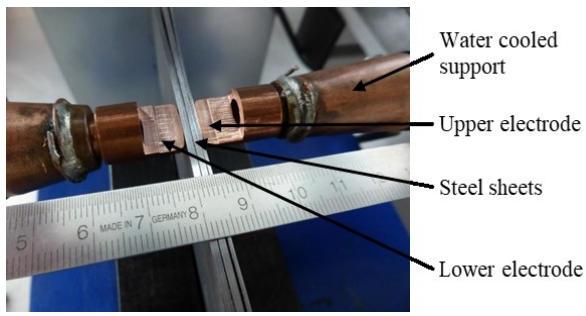

Fig. 2 Half-electrodes squeezed at the stack border of steel sheets.

The IR camera used for the observations is a MW FLIR X6580sc. A microscopic lens with high focal length (300 mm) centres the map only on steel sheets between the electrodes (9.6 mm x 7.68 mm). Temperature measurements, with emissivity evolution, have been achieved on the same device and presented elsewhere [11]. The temperature range is from

20 °C to 600 °C for blackbody temperature. Three integration times are needed to operate on the whole temperature range. Therefore, the effective frequency is 220 Hz, and that corresponds to one image each 4.545 ms with a map at 640 x 256 pitches.

The dissimilar assembly of three-steel sheets considered here is presented in table 1. The combination includes a very thin LCS sheet of 0.57 mm thickness, a 1.47 mm AHSS sheet and a 1.2 mm PHS sheet. The LCS and the AHSS sheets are coated by galvanization. The PHS has an Al-Si coating to resist to hot stamped conditions. More details on this coating are given by Saha *et al.* [12].

Table 1 Stack-up details.

Position	Name	Type	Thickness (mm)	Coating
upper	AM54	LCS	0.57	zinc (10 µm)
center	DP600	AHSS	1.47	zinc (10 µm)
lower	Usibor®1500	PHS	1.2	Al-Si (30 µm)

EXPERIMENTS

To maintain an equivalent current density and contact pressure during half-spot welding, the intensity and the load are split by two (I = 4.5 kA and F = 2 kN), comparatively to the parameters used during classic spot weld configuration (I = 9 kA and F = 4 kN). During the welding time, the current is measured with an electrical shunt and the voltage between electrodes too (Fig. 3).

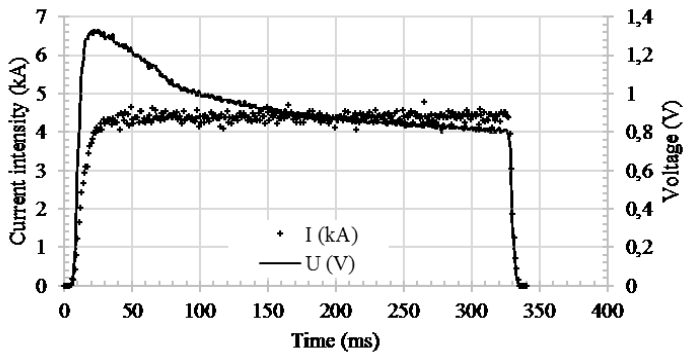

Fig. 3 Experimental current intensity and voltage in half-spot welding.

On the first IR image (Fig. 4), the two electrodes, the three-steel sheets and the four interfaces can be identifyed.

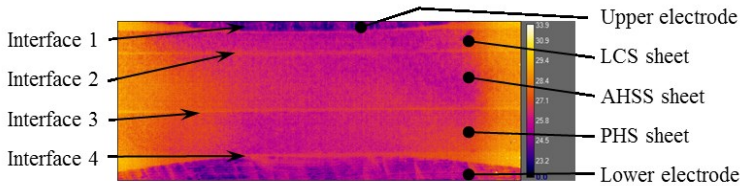

Fig. 4 Initial IR image at t = 0 ms.

The IR camera recording is synchronised with current and voltage measurements through a numerical data recorder. The vertical dashed red lines in Fig. 5 represent the times for the different recorded images in Fig. 6.

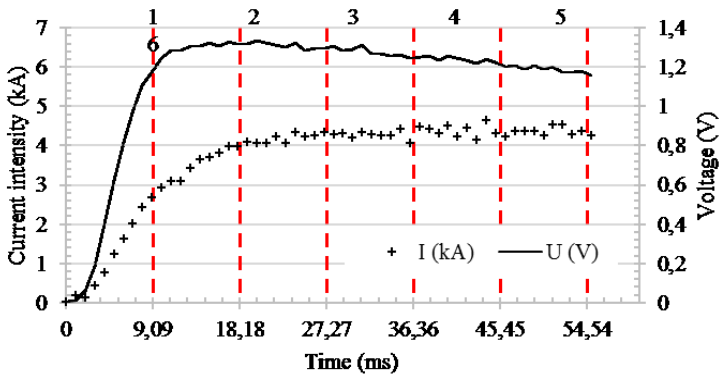

Fig. 5 Current intensity and voltage versus time for six IR images.

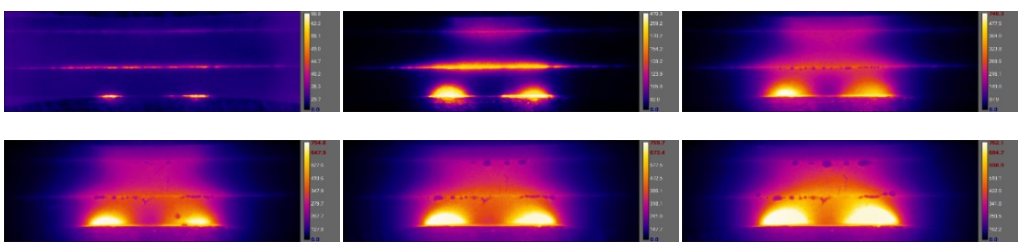

Fig. 6 IR images at different times.

On the IR images, the interfaces 3 and 4 (Fig. 4) from either side of PHS sheet that react from 9.09 ms appear clearly. The fusion of zinc coating appears with small coolest drops at the interface. The drops are visible at 27.273 ms between AHSS and PHS sheets and at 36.364 ms between LCS and AHSS sheets.

The heating at the interface 4 between PHS sheet and electrode is localised on the external of the contact. This is due to the non-uniform current density distribution in revolution geometry providing higher current density at the extremities of the contact area.

NUMERICAL SIMULATION

NUMERICAL MODEL

The numerical model is a coupled electro-thermal finite element model with a 2D axisymmetric geometry. The governing equation for the electrical problem is the current density conservation:

$$div\,\vec{J} = 0 \tag{1}$$

where J ($A \cdot m^{-2}$) is the current density calculated according to:

$$\vec{J} = -\sigma \cdot \nabla V \tag{2}$$

where σ ($S \cdot m^{-1}$) is the electrical conductivity.
The heat generation due to Joule effect is calculated with:

$$Q_J = \frac{1}{\sigma} J^2 = \sigma \cdot (\nabla V)^2 \tag{3}$$

The governing equation for thermal problem is the following heat equation:

$$\rho c \frac{\partial T}{\partial t} = \nabla \cdot (k \nabla T) + Q_J \tag{4}$$

where T (K) is temperature, t (s) is time and k ($W \cdot m^{-1} \cdot K^{-1}$), ρ ($kg \cdot m^{-3}$) and c ($J \cdot kg^{-1} \cdot K^{-1}$) are respectively the thermal conductivity, the density and the specific heat of materials. The latent heat of change phase is taken into account with equivalent specific heat.

For the electrical boundary conditions, the current density J is imposed at the top of the upper electrode with the current value I measured in half-spot welding multiplied by two. The potential 0 V is imposed at the bottom of the lower electrode. For the thermal boundary conditions, exchanges with the environment are assumed negligible and therefore adiabatic conditions are considered.

The mesh is composed of triangular quadratic elements (Fig.7). The maximum size of the elements is imposed: 50 µm at the interfaces, 100 µm in steel sheets between electrodes and 1 mm for the rest of the geometry.

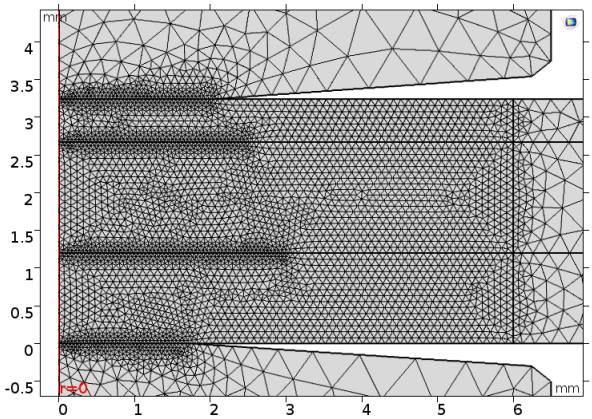

Fig. 7 Meshing in the interest areas.

CONTACT CONDITIONS

Due to indentation of the rounded tip electrodes inside the sheets, the contact radii at electrode-sheet (E/S) and sheet-sheet (S/S) interfaces increase during the welding stage. Without a coupled mechanical analysis, the contact radii evolutions cannot be calculated directly by the electro-thermal model. The deformations of the sheets induced mainly by thermal dilatation and indentation of electrodes neither. In our electro-thermal model, contact radii of each interfaces are imposed during 10 ms before to evolve. We assume dilatation and indentation phenomena are negligible before 50 ms.

Measurements of the two E/S contact radii evolutions have been achieved after the squeezing stage and at different interrupted welding times [13] (Fig. 8).

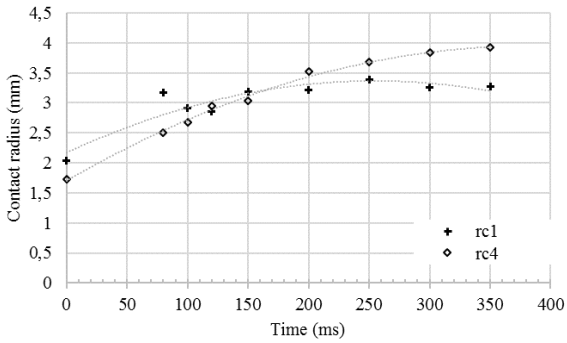

Fig. 8 Experimental evolutions of the electrode-sheet contact radii.

The evolution of E/S contact radii could be represented by a polynomial law (5.1) and (5.2), which are used to calculate rc_1 and rc_4 at 0 ms, 10 ms, 20 ms, 30 ms, 40 ms, and 50 ms.

$$rc_1 = -1.85\times10^{-5}t^2 + 9.41\times10^{-3}t + 2.04 \tag{5.1}$$

$$rc_4 = -1.52\times10^{-5}t^2 + 1.17\times10^{-2}t + 1.73 \tag{5.2}$$

Initial S/S contact radii are respectively 2.52 mm and 3.03 mm, but we have no mean to measure these values until 50 ms. From the initial measurements of S/T contact radii, we assume the ratio between rc_1 and rc_2 and, rc_3 and rc_4 are constant until 50 ms:

$$rc_2 = 1.25\,rc_1 \tag{5.3}$$

$$rc_3 = 1.80\,rc_4 \tag{5.4}$$

We obtain the evolution of contact radii each 10 ms following the graph presented in Fig. 9.

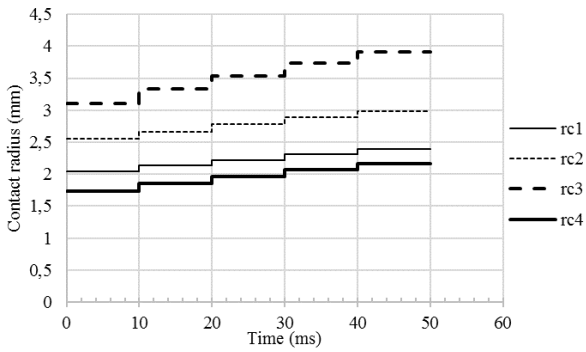

Fig. 9 Contact radii evolutions imposed in the model.

The electrical contact resistances (ECR) and thermal contact resistances (TCR) encountered in this very dissymmetrical stack-up have been measured versus pressure and temperature on a specific device (Fig. 10).

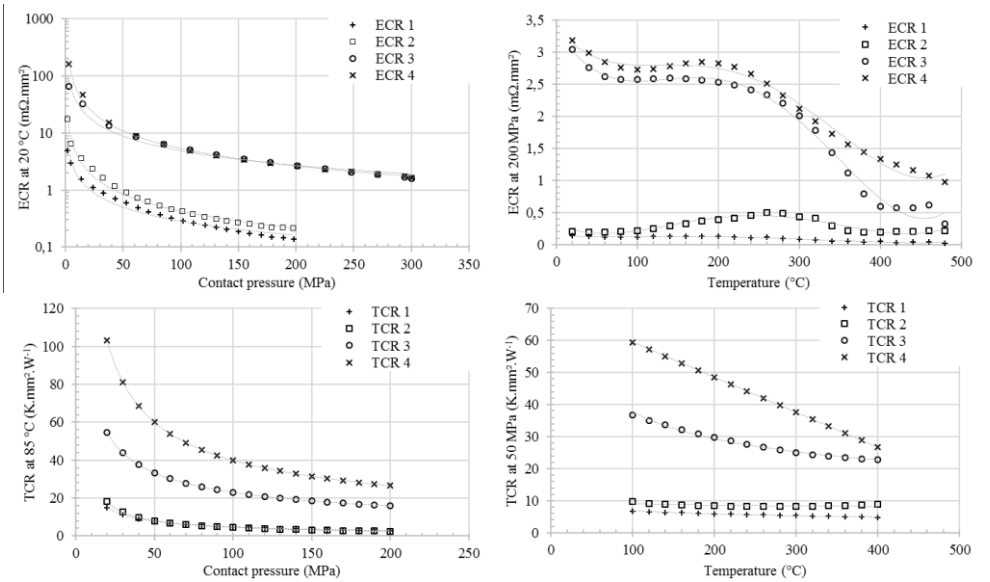

Fig. 10 Electrical and thermal contact resistances evolutions measured on a specific device versus contact pressure and temperature [13], [14].

The contact resistances could be separated in two groups: the zinc coated interfaces and the aluminized interfaces. The intermetallic components formed during the heat treatment of PHS sheet by diffusion of iron in aluminum-silicon (Al-Si) contribute to increase drastically the electrical resistivity of the coating. The resistance of the Al-Si layer is included in the contact resistance values [14].

To be embedded properly in the model, experimental evolutions should be fitted with a phenomenological law. We suppose ECR and TCR evolutions follow a law with separable variables as Srikunwong [15]:

$$ECR(p_c, T_c) = f(T_c)\, g(p_c) \tag{6.1}$$

$$TCR(p_c, T_c) = f'(T_c)\, g'(p_c) \tag{6.2}$$

Measurements versus contact pressure at room temperature allowed defining a law for $g(p_c)$ and $g'(p_c)$ as a power function of contact pressure:

$$g(p_c) = R_0\, p_c^{-n} \tag{7.1}$$

$$g'(p_c) = R_0'\, p_c^{-n'} \tag{7.2}$$

With the coefficients n and n' close to 1, we assume we can calculate the ECR and TCR evolutions at the contact pressure p_c from the reference pressure p_{ref} (8.1 and 8.2).

$$ECR(p_c, T_c) = ECR(p_{ref}, T_c)\frac{p_{ref}}{p_c} \tag{8.1}$$

$$TCR(p_c, T_c) = TCR(p_{ref}, T_c)\frac{p_{ref}}{p_c} \tag{8.2}$$

The contact pressure and the correction pressure ratio are automatically calculated from the contact radii. Furthermore, the contact resistances evolutions for the aluminized interfaces have been extrapolated at high temperature, until the fusion temperature (1 000 °C) of the Al-Si layer (Fig. 11).

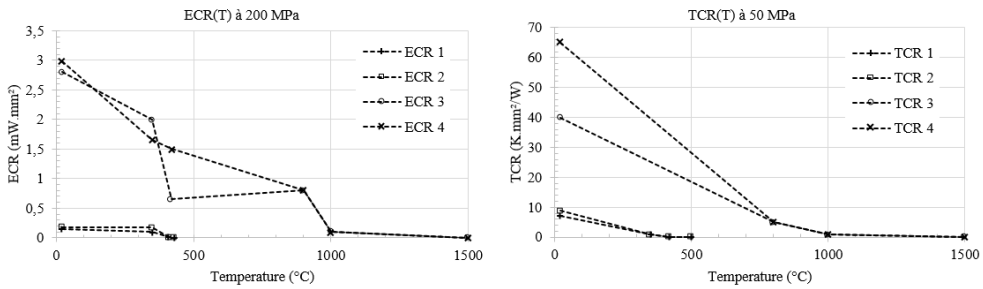

Fig. 11 Extrapolation of the electrical and thermal contact resistances evolution versus temperature at reference pressure for the aluminized interfaces.

RESULTS AND DISCUSS

The calculation time takes 10 min with a standard desktop computer (Intel® Core™ i3-3120M and 8 Go RAM) and less than 5 min with a calculation computer.

Fig. 12 presents the numerical temperature distribution, which is similar to the experimental observations done by IR thermography (Fig 6). The first hot areas are localised on either side of PHS sheet where is Al-Si coating. The red arrows represent the heat flux and their size is proportional to the energy quantity transmitted by conduction. Isothermal lines of coating fusion temperature are drawn in black. They correspond to 420 °C and 1 000 °C for zinc and Al-Si after heat treatment respectively. The white line represents the fusion zone as the isothermal 1 460 °C line.

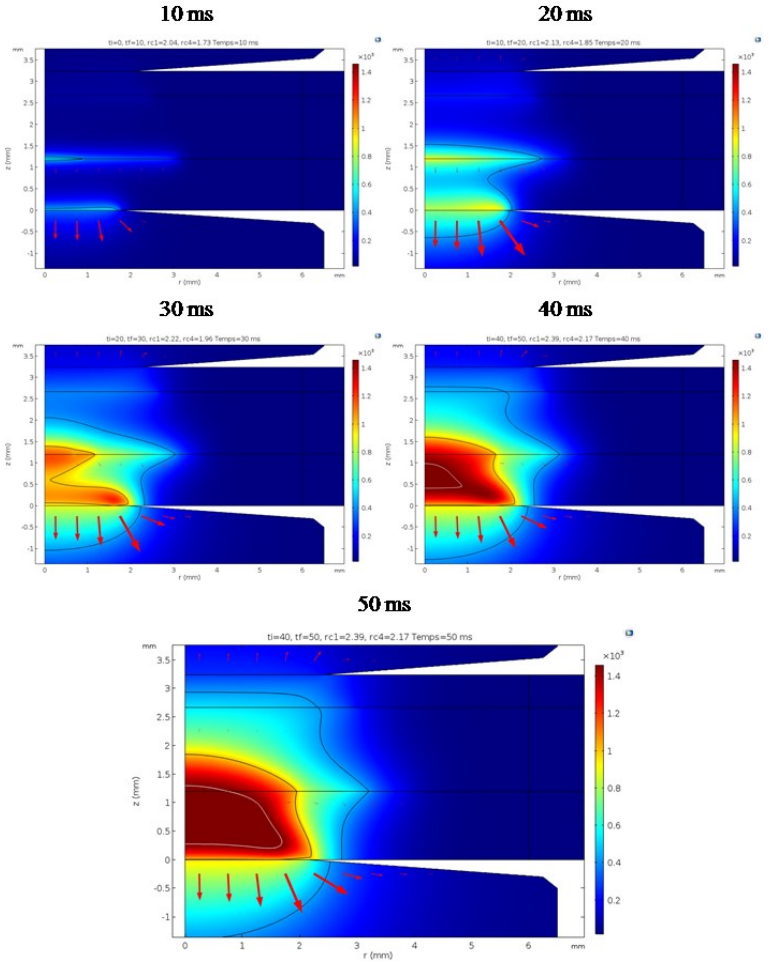

Fig. 12 Temperature distribution from numerical simulation each 10 ms.

The temperature is heterogeneous on the interfaces. On the fourth interface (PHS/Electrode), the hottest point is at the extremity of contact where the current density is higher (Fig. 13). On the third one (AHSS/PHS), the hottest point is on the *z*-axis probably because of lower heat losses at this location.

Unlike experimental observations, a fusion zone is present in the PHS sheet at 40 ms. In half-spot configuration, a large part of energy is lost through the free area by radiation, which contributes to reduce the temperature and delays the melting of sheets.

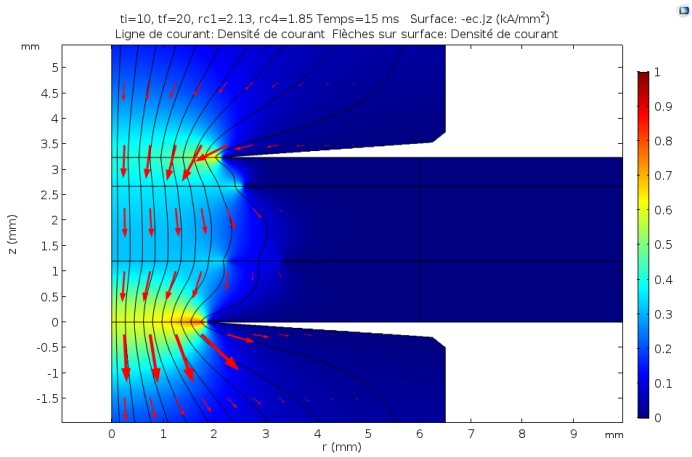

Fig. 13 Current density distribution at 15 ms.

On the IR image at 36 ms, some drops appear at LCS/AHSS interface (Fig.14). They correspond to zinc coating fusion and give information on the contact temperature. On the equivalent numerical temperature repartition, we find the isotherm at 420 ° C at the same interface and at the same moment.

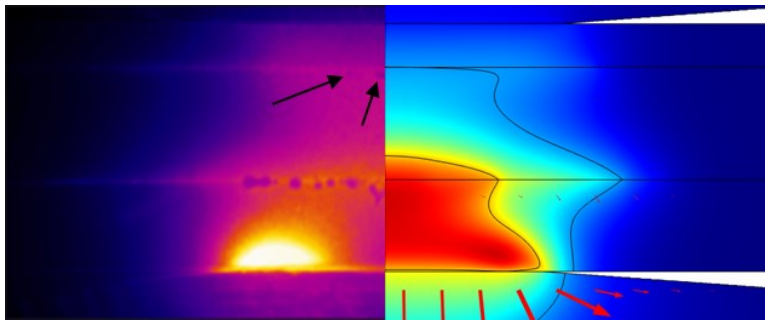

Fig. 14 Comparison between infrared image and numerical simulation at 36 ms.

Even if the model cannot be used beyond 50 ms, the comparison between the experimental nugget at 80 ms and the numerical simulation at 50 ms give similarities (Fig. 15). Firstly, the distance between the fusion zone and the lower electrode is equal. This distance is driven by the cooling of nugget by the electrode. The numerical values of contact areas and of thermal contact resistances are of the same order of magnitude than the experimental ones. Secondly, the shape and the size of the fusion zone and the heat affected zone are consistent between numerical simulation and experimental macrograph.

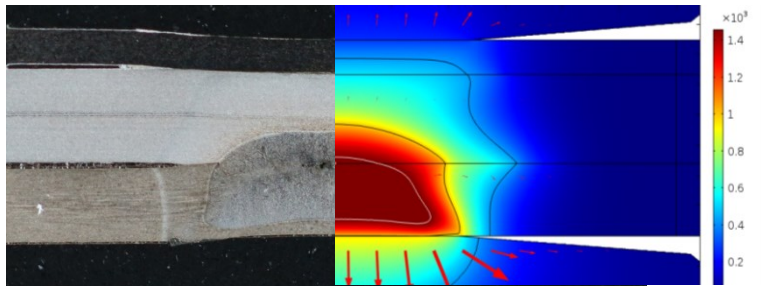

Fig. 15 Comparison between macrographic image at 80 ms and numerical temperature distribution at 50 ms.

The contact temperature on the *z*-axis is presented in Fig. 16. It can be seen that the zinc fusion temperature as the interface 2 is reached at 36 ms as already observed in Fig. 14. The contact temperatures *Tc1* and *Tc2* slowly increase, while *Tc3* and *Tc4* reach 800 °C in 16 ms and 21 ms, respectively. The temperature *Tc4* is saturated at 1 000 °C due to the cooling of the electrodes. The heating speed are reported in Table 2.

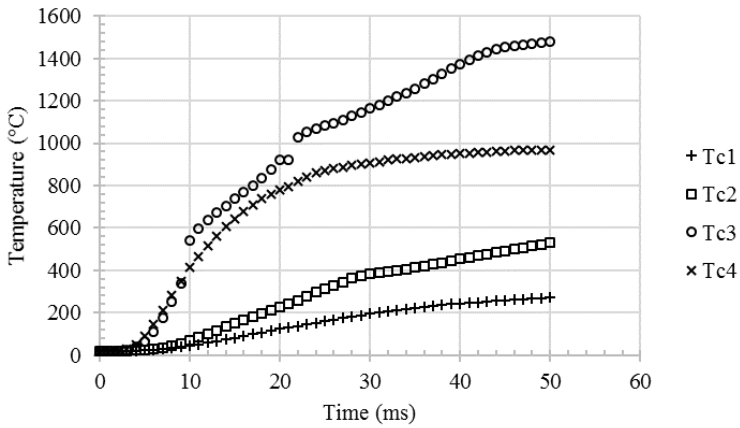

Fig. 16 Contact temperatures versus time on the symmetrical axis.

Table 2 Heating speed of contact temperatures in °C/ms.

Tc1	***Tc2***	***Tc3***	***Tc4***
7	16	94 – 35 – 19	55

The three values for the *Tc3* correspond to the three stages seen Fig. 16, respectively, on the ranges [5 ms – 11 ms], [10 ms – 19 ms] and [22 ms – 40 ms]. The heating speed at the interface between AHSS and PHS has been measured by IR thermography [11]. The experimental value, 40 °C/ms, is very close to the value obtain with the numerical model in the range [10 ms – 19 ms] where 35 °C/ms is calculated (Table 2).

Finally, the numerical voltage between the electrodes could be compared with the experimental one. It permits to assess the coherence of the contact radii and the electrical

contact resistances. Fig. 17 presents the experimental and the numerical voltage between the two electrodes. The curves are very close until 8 ms then the simulation gives weaker values until 20 ms. The change of slop occurs before the change of contact radius. It seems like the difference comes from the electrical contact resistance, which had a lower value.

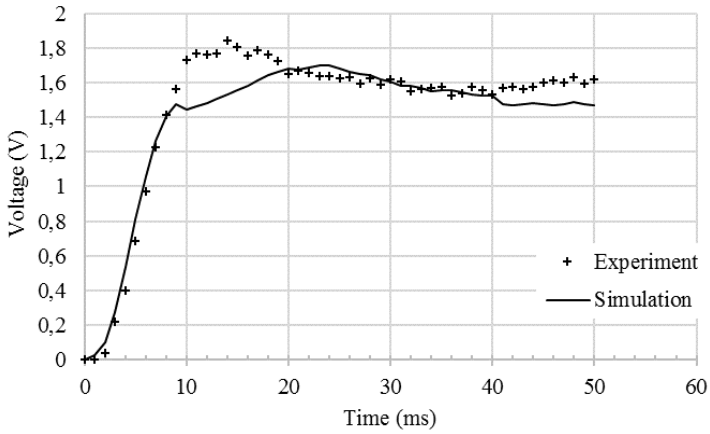

Fig. 17 Experimental and numerical voltage between electrodes.

CONCLUSION AND PROSPECT

The evolution of contact radii in the first 50 ms show a lot of information during the initial heating that occurs in the resistance spot welding process in the presence of a PHS sheet with Al-Si coating in hot stamped conditions. In a stack-up including a very thin zinc coated Low Carbon Steel sheet, a zinc coated Advanced High Strength Steel sheet, and an Al-Si coated Press Hardened Steel of 0.57 mm, 1.47 mm, and 1.2 mm thicknesses, respectively, the initial overheating occurs on either side of PHS sheet. The melted area initiates directly in the Al-Si coated sheet then grows toward the top of the assembly.

The simply electro-thermal model developed in this study permits in 10 min of calculation time to identify the causes of overheating. The Al-Si coating is very resistive after the heat treatment for hot stamping. The current density is also a key parameter and the difference of contact radius at two electrode-sheet contacts focusses the heating on the side of the hardest sheet.

Several models of resistance spot welding include mechanical calculation at the expense of calculation time. But in the first 50 ms, dilatation phenomena are negligible, and the contact radii can be imposed from some experimental investigations.

This model can be adapted to other assemblies and with other coatings. However, new experimental characterization of contact resistance would be necessary even if the experimental temperature measurements by infrared camera allows to validate the models.

REFERENCES

[1] C. V. NIELSEN, K. S. FRIIS, W. ZHANG, AND N. BAY: 'Three-Sheet Spot Welding of Advanced High-Strength Steels', *Welding Research*, vol. 90, February, pp. 32s–40s, 2011.

[2] N. HUDA AND Y. PARK: 'Weldability Evaluation and Nugget Formation Mechanism in Three Sheets Spot Welding of High Strength Steels', *Welding Research*, *Proceedings of the 9th International Conference*, Chicago, Illinois, USA, pp. 680–684, 2012.

[3] J. A. KHAN, L. XU, AND Y. J. CHAO: 'Prediction of nugget development during resistance spot welding using coupled thermal–electrical–mechanical model', *Science and Technology of Welding and Joining*, vol. 4, no. 4, pp. 201–207, 1999.

[4] S. S. BABU, M. L. SANTELLA, Z. FENG, B. W. RIEMER, AND J. W. COHRON: 'Empirical model of effects of pressure and temperature on electrical contact resistance of metals', *Science and Technology of Welding and Joining,* vol. 6, no. 3, pp.126-132, 2001.

[5] E. FEULVARCH, V. ROBIN, AND J. M. BERGHEAU: 'Resistance spot welding simulation: A general finite element formulation of electrothermal contact conditions', *Journal of Materials Processing Technology*, vol. 153–154, no. 1–3, pp. 436–441, 2004.

[6] P. S. WEI AND T. H. WU: 'Electrical contact resistance effect on resistance spot welding', *International Journal of Heat and Mass Transfer*, vol. 55, no. 11–12, pp. 3316–3324, 2012.

[7] R. N. RAOELISON, A. FUENTES, P. ROGEON, P. CARRÉ, T. LOULOU, D. CARRON, AND F. DECHALOTTE: 'Contact conditions on nugget development during resistance spot welding of Zn coated steel sheets using rounded tip electrodes', *Journal of Materials Processing Technology*, vol. 212, no. 8, pp. 1663–1669, 2012.

[8] R. N. RAOELISON, A. FUENTES, C. POUVREAU, P. ROGEON, P. CARRÉ, AND F. DECHALOTTE: 'Modeling and numerical simulation of the resistance spot welding of zinc coated steel sheets using rounded tip electrode: Analysis of required conditions', *Appl. Math. Model.*, vol. 38, no. 9–10, pp. 2505–2521, 2014.

[9] P. ROGEON, P. CARRÉ, J. COSTA, G. SIBILIA, AND G. SAINDRENAN: 'Characterization of electrical contact conditions in spot welding assemblies', *Journal of Materials Processing Technology*, vol. 195, no. 1–3, pp. 117–124, 2008.

[10] U. FÜSSEL, V. WESLING, A. VOIGT, AND E. C. KLAGES: 'Visualisierung der Temperaturentwicklung in der SchweiSzone einschlieSlich der SchweiSelektroden über den gesamten zeitlichen Verlauf eines PunktschweiSprozesses', *Schweissen und Schneiden*, vol. 64, pp. 634–642, 2012.

[11] E. GESLAIN, T. PIERRE, P. ROGEON, C. POUVREAU, AND L. CRETTEUR: 'Contact temperature measurement by infrared thermography during resistance spot welding process', *QIRT*, Berlin, 2018.

[12] D. C. SAHA, C. W. JI, AND Y. D. PARK: 'Coating behaviour and nugget formation during resistance welding of hot forming steels', *Science and Technology of Welding and Joining*, vol. 20, no. 8, pp. 708–720, 2015.

[13] E. GESLAIN: *Soudage par résistance des tôles fines revêtues : formation du noyau dans un assemblage de trois tôles*, thesis, Université Bretagne Sud, 2018.

[14] E. GESLAIN, P. ROGEON, T. PIERRE, C. POUVREAU, AND L. CRETTEUR, "Coating effects on contact conditions in resistance spot weldability," *Journal of Materials Processing Technology*, vol. 253, pp. 160–167, 2018.

[15] C. SRIKUNWONG : *Modélisation du procédé de soudage par points*, thesis, Ecole des Mines de Paris, 2005.